Eur. Phys. J. B (2015)
DOI: 10.1140/epjb/e2015-60543-1

THE EUROPEAN PHYSICAL JOURNAL B

Regular Article

The stability and interfacial properties of functionalized silica nanoparticles dispersed in brine studied by molecular dynamics

Lucas S. de Lara[1,2], Vagner A. Rigo[1,3], and Caetano R. Miranda[1,4,a]

[1] Centro de Ciências Naturais e Humanas (CCNH), Universidade Federal do ABC (UFABC), Santo André, SP, Brazil
[2] Universidade Estadual de Ponta Grossa (UEPG), Ponta Grossa, PR, Brazil
[3] Universidade Tecnológica Federal do Paraná (UTFPR), Cornélio Procópio, PR, Brazil
[4] Instituto de Física, Universidade de São Paulo (IF-USP), São Paulo, SP, Brazil

Received 4 July 2015 / Received in final form 7 September 2015
Published online (Inserted Later) – © EDP Sciences, Società Italiana di Fisica, Springer-Verlag 2015

Abstract. The charge accumulation and surface tension of overall neutral functionalized silica nanoparticles (NPs) dispersed in brine (NaCl and $CaCl_2$) were studied using large scale fully atomistic molecular dynamics. Sulphonic (SA) and ethylene-glycol (EG) functional groups have been incorporated in the NP surface respectively, covering both the hydrophobic and hydrophilic characters. For the latter, groups with one (EG) and two (PEG2) monomers were considered. The ion distribution in electrolyte aqueous solution and its accumulation around NPs were monitored for different salt concentrations (from 0.05 up to 1 wt%), and temperature (300 and 350 K) at 1 atm. At certain conditions, the ion accumulation surrounding the overall neutral NPs leads to a formation of electrical double layers (EDL). Compared with the monovalent ions (NaCl), the accumulation of divalent ions ($CaCl_2$) was found to be more pronounced and the thickness of the EDL around the NPs is more compact. According to the functional group attached, the EDL width also reduces going from EG, to PEG2, to SA. Our simulations suggest that the EDL formation, its narrowing, the large variation of the interface tension, followed by a steep increase in ion mobility are conditions which may precede instability of functionalized NPs dispersion in brine.

1 Introduction

The use of SiO_2 nanoparticles (NPs) to control and modify the properties of fluids and interfaces is a growing interest area in interfacial science. The high versatility of silica NPs provides a broad range of applications ranging from drug delivery [1,2] and diagnostics [2,3], in the biomedical area to developing hydrophobic surfaces [4–11], lubricant additives [12], and enhanced oil recovery (EOR) in petroleum fields [13–17].

The NP stabilization in the fluid media is a key factor to maintain dispersion, as a suspension collapse can cause property degradation and eventual damage through the formation of a solid aggregate due to the NP precipitation. For EOR applications, the injection of NPs into oil reservoirs represents a particular challenge due to the harsh downhole environments for NP stabilization [17]. In these cases, the dispersion can quickly become unstable and agglomerate when the nanofluid is exposed to different pH [13], salinity and/or temperatures [13]. A dispersion collapse is undesirable because the precipitate can damage the reservoir and block the porous rock, hindering the EOR process.

For highly charged surfaces within electrolyte solution, the formation of an electrical double layer (EDL) surrounding the NP represents an important factor for the NP suspension, where the electric force is balanced by the van der Waals interactions [18–20]. In this direction, Jenkins et al. [21–23] evaluated the interaction of two silica NPs in an aqueous media for monovalent electrolyte concentrations where surface charged sites were introduced in the NPs by considering deprotonated sites on the NP surface. Variations in the inter-particle force were reported when there is a variation in the number of charged sites. However, for a fixed number of charged sites the authors also found that the inter-particle force changed for different electrolyte concentrations. This effect points out for a more elaborated origin of the inter-particle force.

However, the EDL formation was also reported for overall neutral NPs in electrolyte solutions [24]. Our recent study considered molecular dynamics (MD) simulations with a hydroxylated (neutral) silica NP in the electrolyte solution, showing differences in the surface tension for solutions of mono- (NaCl) and divalent ($CaCl_2$) salts [16]. Also using MD, de Lara et al. showed narrowing effects for EDL's composed by different salts, surrounding an overall neutral H-passivated silica NP [25]. These results reinforce that effects, such as hydrophobicity/hydrophilicity and hydrogen bond network of water molecules on NP surface must be taken into account to the EDL formation [26–28]. To focus on the effects of the functionalized sites over the ion distribution and water molecules network, deprotonated sites are not explicitly considered in

[a] e-mail: cmiranda@if.usp.br

Table 1. Concentration (in wt% and χ_i mole fraction) and number of ions and molecules for each evaluated system.

NaCl solution						
Temperature and pressure	Salt wt%	χ_{Na} ($\times 10^{-3}$)	χ_{Cl} ($\times 10^{-3}$)	χ_S ($\times 10^{-3}$)	Na/Cl (ions)	H_2O (molecules)
300 and 350 K; 1 atm	0.05	0.1562	0.1562	0.1562	5/5	31 992
	0.10	0.3124	0.3124	0.3125	10/10	31 989
	0.25	0.7808	0.7808	0.7822	25/25	31 968
	0.50	1.4985	1.4985	1.5007	48/48	31 936
	1.00	2.9940	2.9940	3.0030	96/96	31 872
$CaCl_2$ and $MgCl_2$ solutions						
	Salt wt%	$\chi_{Ca/Mg}$ ($\times 10^{-3}$)	χ_{Cl} ($\times 10^{-3}$)	χ_S ($\times 10^{-3}$)	Ca(Mg)/Cl (ions)	H_2O (molecules)
300 and 350 K; 1 atm	0.05	0.0628	0.1255	0.0628	2/4	31 852
	0.10	0.1569	0.3138	0.1570	5/10	31 845
	0.25	0.3768	0.7536	0.3771	12/24	31 810
	0.50	0.7850	1.5701	0.7863	25/50	31 771
	1.00	1.5070	3.0140	1.5116	48/96	31 707

NP models [25]. In this way, the potential of zero charge (PZC) of the nanoparticle is fixed and pH variations are not allowed in the system. These models allow us to evaluate the ion distribution when the electrostatic force is not the only main driving force acting.

The surface functionalization is a common way to avoid NP precipitation [29]. For an NP in an aqueous electrolyte solution, hydrophobic and hydrophilic functional groups are actually considered to avoid precipitation [15,30,31]. In this direction, Sondjaja et al. [31] showed that the interaction of hydrophilic molecules (polyethylene oxide) with an electrolyte solution can result in the formation of a nanoaggregate. Particularly, the study of functionalized NPs within electrolyte solutions can illuminate the problem of the EDL formation in overall neutral NPs. In a previous work of the present authors, the energetics of formation and hydration of functionalized silica nanoparticles have been studied by MD [30]. The results have shown that surface functionalization and water arrangement plays a central role in the energetics and structural properties of these systems.

In this present study, we investigate amorphous silica NPs functionalized by organosilane molecules whose radical contains: (i) ethylene-glycol; and (ii) sulfonic terminations. These functional groups represent hydrophilic and hydrophobic nanoparticle coverage, respectively. Furthermore, these groups are able to modify the silica nanoparticle surface and the dispersion properties, as shown by Metin et al. in a recent experimental study [15]. The functionalized NPs were evaluated in mono (NaCl) and divalent ($CaCl_2$) electrolyte solutions, using MD simulations. The ion distributions were monitored through salt concentrations from 0.05 up to 1 wt%, and temperatures of 300 and 350 K at 1 atm.

2 Materials and methods

The systems were simulated using the Large-Scale Atomic/Molecular Massively Parallel Simulator (LAMMPS) code [32]. The CHARMM-based interatomic potential of Cruz-Chu et al. [33] was used to describe the interactions in the SiO_2 system and functional groups, employing the Lorentz-Berthelot mixing rules [34,35]. A non-rigid bulk version of this model that includes bond stretching and angle bending parameters was also used [36]. Water molecules were described using the SPCE/FH potential [37]. Coulomb and van der Waals interactions were included for salt ions. The initial structure and charges for functional groups were obtained from reference [30].

The atomistic models of hydroxylated silica NPs (NP-H) were generated using a scheme based on the Monte Carlo Method [38]. The resulting NP-H presents an approximately spherical shape with a diameter of 3 nm. The hydrophobic and hydrophilic terminations are given by adding the functional groups $Si(OH)_3$-$(CH_2)_3$-SO_3H (SA) and $Si(OH)_3$-$(CH_2$-CH_2-$O)_n$-H (ethylene-glycol), respectively. For NPs grafted with ethylene-glycol, systems with $n = 1$ and 2 (EG and PEG2) monomers were considered. These NP generation and graft processes are the same as adopted in a previous work [30].

The electrolyte aqueous solutions were equilibrated to obtain the configurations with different salt concentrations (NaCl or $CaCl_2$). The ions were inserted randomly, keeping the charge neutrality of the system by replacing water molecules. The simulations used a cubic box of 10 nm per side. In order to insert the functionalized silica NP after the equilibration process, a spherical void was created at the center of the system. Table 1 presents the number of water molecules and ions for each evaluated system. The NP-H, NP-SA, NP-EG, and NP-PEG2 have 1083, 2256, 1856, and 2060 atoms, respectively.

For each system, simulations were performed in three stages. In the first one, to equilibrate the translational and vibrational degrees of freedom, the system evolved for 1.0 ns in the NVT ensemble. A subsequent simulation of 4.0 ns in the NPT ensemble was used to equilibrate the system under target temperature and pressure conditions (300 K or 350 K and 1 atm). Finally, the system evolved for 8.0 ns in the NVT ensemble, with the volume

fixed at the average of the previous NPT simulation. For long-range electrostatic interactions, the reciprocal space Particle Particle Particle-Mesh (PPPM) method [39,40] was adopted. In all calculations, a timestep of 0.5 fs and a cutoff of 10.0 Å were used for the van der Waals interactions. Temperature and pressure were controlled by the Nose-Hoover thermostat [41,42] and the Andersen barostat [43], respectively.

The charge ion distribution surrounding the NP is the main property to describe the electrostatic behavior of these systems. A simplified molecular picture of the ion complexation surrounding an NP surface can be seen in Figures 1a–1c. Figure 1a shows a number of shells around the NP, from which the net number of ions were computed. Figure 1b shows an enlarged view of Figure 1a, where the NP and the Stern layer are shown in detail. The positions of the surface charges that form the NP-H $\sigma_{\rm sh}$, and $\sigma_{\rm bulk}$) and functional sites ($\sigma_{\rm func}$) are indicated, respectively. Figure 1c shows a molecular representation of the NP-SA surface, which contains details of the partial charges. Similarly, Figures 1d and 1e present details of the EG and PEG2 groups on the NP surface.

The electrostatic analysis of two regions (Stern and diffuse) were used to characterize the NP within the electrolyte aqueous solution at different salt concentrations. The definition of the Stern and diffuse regions is consistent with a previous work [25], where the Stern region is considered by taking into account the effective NP radius, i.e. the NP with the functional groups on the surface. The Stern layer extends up to 10 Å from the NP surface. The histograms of the charge distribution, as function of the distance r from the NP center of mass, were obtained by considering a layer Δr around r. The ion distribution around the NP was determined by time-averaging the ion position in a total of 1000 configurations, using a of 1 ps time lag between each. The layer size Δr is defined as $\Delta r(l) = R_{\rm max}/l$, where $R_{\rm max}$ is the maximum radius in the simulation and the number of layers l was chosen as 200.

The charge distribution can be obtained from the ion distribution, considering the charge of each ion. For each layer its total charge is given by:

$$q_{+,-}(r) = \frac{1}{N\Delta r(l)} \sum_{i=1}^{N} (r_i - r_{cm})^{1/2} q_i, \qquad (1)$$

where N is the total number of atoms.

Based in a procedure described in references [25,44], the net charge due to the ion distribution is used to compute the cumulative net ion charge

$$Q(r) = \frac{F}{|\sigma_s|} \int_0^r [c_+(r) - c_-(r)]dr, \qquad (2)$$

where F is the Faraday constant, $c_+(r)$ or $c_-(r)$ are the positive or negative charge distributions, respectively, defined by $c_{+,-}(r) = q_{+,-}(r)/N(\Delta r(l))^3$, and σ_s is the local surface charge density (Fig. 1).

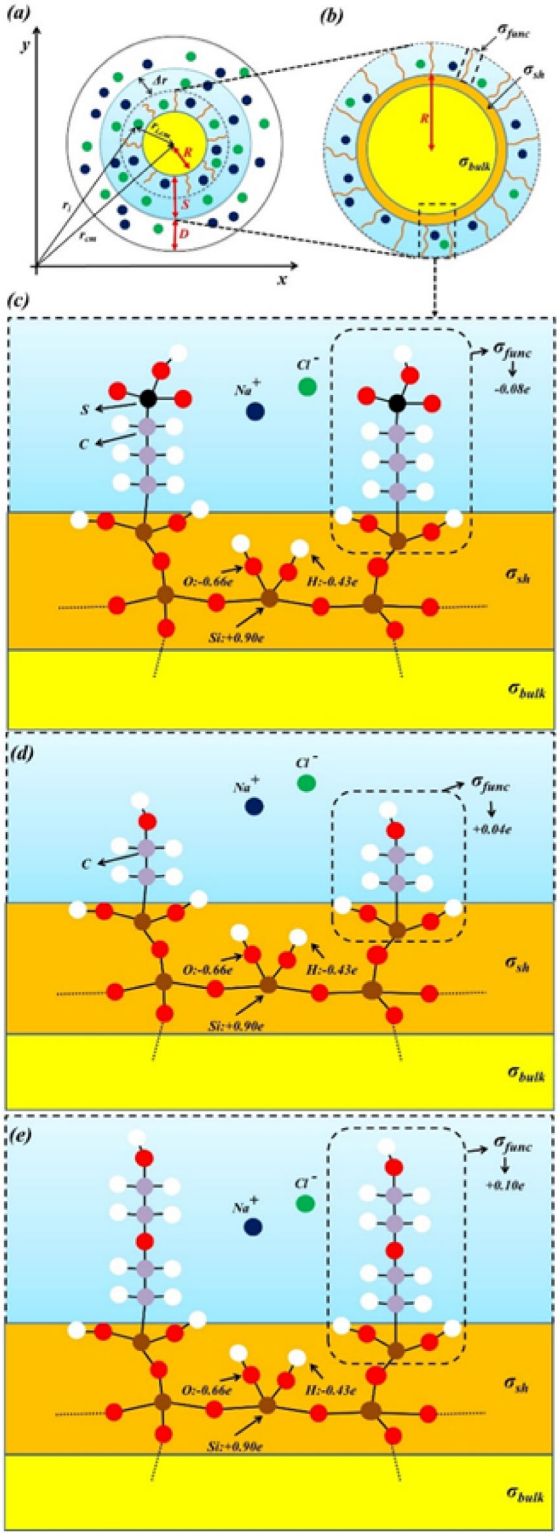

Fig. 1. Schematic representation for a functionalized nanoparticle (NP) in brine: (a) charge distribution around the nanoparticle, where the label R is the nanoparticle radius, and where S and D are the Stern and diffuse regions, respectively. (b) Enlarged view of (a), focusing on the NP and the Stern regions. An enlarged view of the functionalized NP surface is presented in (c), (d), and (e) for NP-SA, NP-EG, and NP-PEG2, respectively, which contains details of the partial charges.

The self-diffusion coefficient was determined through the slope of the mean square displacement ($MSD(t) = \langle (r_i(t) - r_i(0))^2 \rangle$) in the Einstein equation:

$$D = \frac{1}{6} \lim_{t \to \infty} \frac{1}{N} \sum_{i=1}^{N} \frac{MSD(t)}{t}. \quad (3)$$

Considering the spherical symmetry of the NP, the surface tension in the formulation of Gibbs can be given in terms of pressure tensor [25,45–47]:

$$\gamma = \left[-\frac{(P_l - P_g)^2}{8} \int_0^{\infty} r^3 \frac{dP_N(r)}{dr} dr \right]^{1/3}, \quad (4)$$

where the terms P_l and P_g are the internal and external pressures acting on the NP, respectively, and $P_N(r)$ is the normal component of pressure given by

$$P_N(r) = \frac{2}{r^2} \int_0^{r} r P_T(r) dr, \quad (5)$$

where $P_T(r)$ is the tangential component of the pressure tensor.

3 Results and discussion

The results for functionalized NPs within dispersions of monovalent salt (NaCl) are presented in Section 3.1, while Section 3.2 presents the results for NPs in the divalent salt ($CaCl_2$) concentrations. The $Q(r)$ results shown here (Figs. 2a–4b for NaCl, and Figs. 5a– 7b for $CaCl_2$) present two main effects: (i) the sign inversion of the effective charge at the first ion layer according with the salt concentration, and (ii) the EDL formation for some salt concentration. The transport properties for each NP system are presented in Section 3.3, and the surface tension results appear in Section 3.4.

3.1 Functionalized nanoparticles in brine – monovalent salts (NaCl)

The charge distributions $Q(r)$ around the NP-SA are presented in Figures 2a and 2b for 300 and 350 K, respectively. The $Q(r)$ results for both temperatures present some differences: at 350 K (Fig. 2b) the accumulation of ions begins at a greater r (∼20 Å) than at 300 K (Fig. 2a) (∼18 Å). This indicates that at higher temperature, ions can migrate to the nanoparticle shell region due to increase in diffusivity in agreement with observed in the literature [30]. The $Q(r)$ intensity is attenuated in the Stern region and enlarged in the diffuse region in tandem with the temperature increase, which is clearly shown in Figures 2a and 2b for 1 and 0.50 wt% curves for both temperatures. The comparison of $Q(r)$ for different concentrations at 300 K (Fig. 2a) indicates that variations in the salt concentration provide a sign inversion of the effective charge observed at the first ion layer. This charge inversion occurs between 0.50 wt% (accumulation of Cl^- ions) and 1 wt% (accumulation of Na^+ ions). At 350 K (Fig. 2b) the inversions of $Q(r)$ close to the NP surface (between 20–23 Å) occur between 0.05 and 0.10 wt%. Other inversions occur between 0.10 and 0.25 wt% and between 0.25 and 0.50 wt%. The evolution of $Q(r)$ for each salt concentration shows the formation of an electrical double layer (EDL) at 0.25 and 1 wt% at 300 K. However, at these concentrations, the total cumulative charge remains with negative and positive values, indicating a frustrated screening. This effect can be understood given the fact that in the NP-SA surface, after the functionalization processes, some silanol groups still remain, and both hydrophobic and hydrophilic sites are available [30]. At 350 K the $Q(r)$ for 0.10 wt% presents the accumulation of Cl^- ions up to approximately 26 Å, while for distances greater than 29 Å the accumulation of Na^+ ions occurs, reaching a net positive accumulated charge after 30 Å. This effect indicates the formation of an EDL in this system.

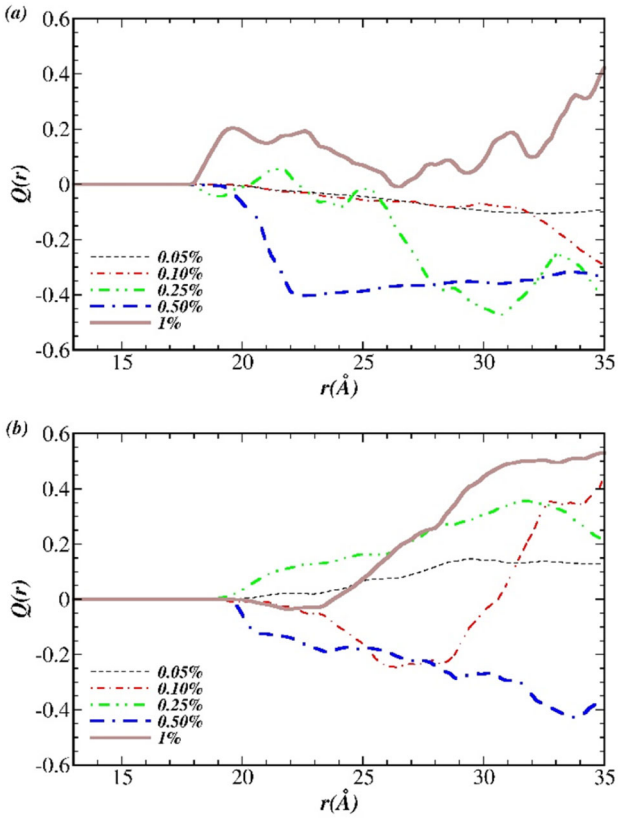

Fig. 2. The respective cumulative net ion charge ($Q(r)$) at (a) 300 and (b) 350 K for an NP-SA in brine (NaCl solutions).

Figures 3a and 3b present the $Q(r)$ distribution around the NP-EG center of mass at 300 and 350 K, respectively. At 300 K, salt concentrations of 0.05 and 0.10 wt% provide the formation of a negative (Cl^- accumulation) layer from 20 up to 35 Å. For greater salt concentrations there is a slight accumulation of Cl^- ions close to 20 Å (except

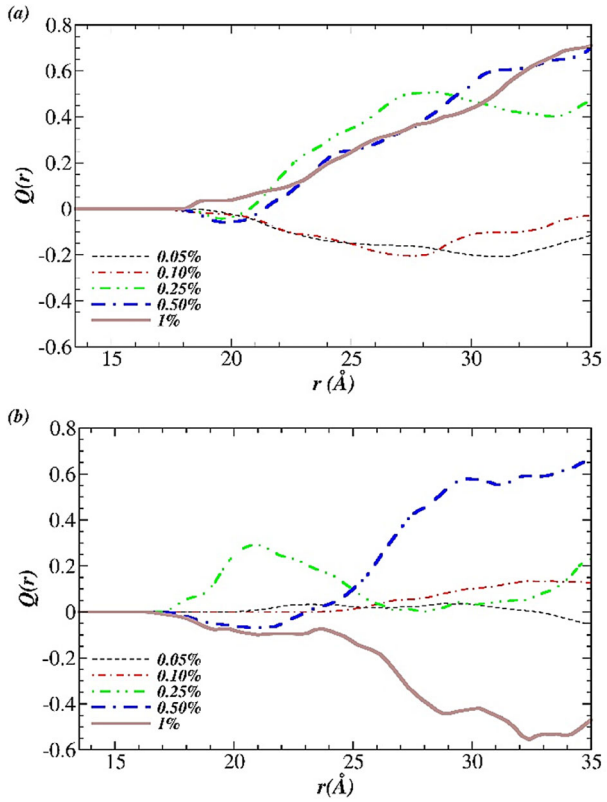

Fig. 3. Cumulative net ion charge around the NP-EG center of mass at (a) 300 and (b) 350 K, for an NP-EG in the brine (NaCl solution).

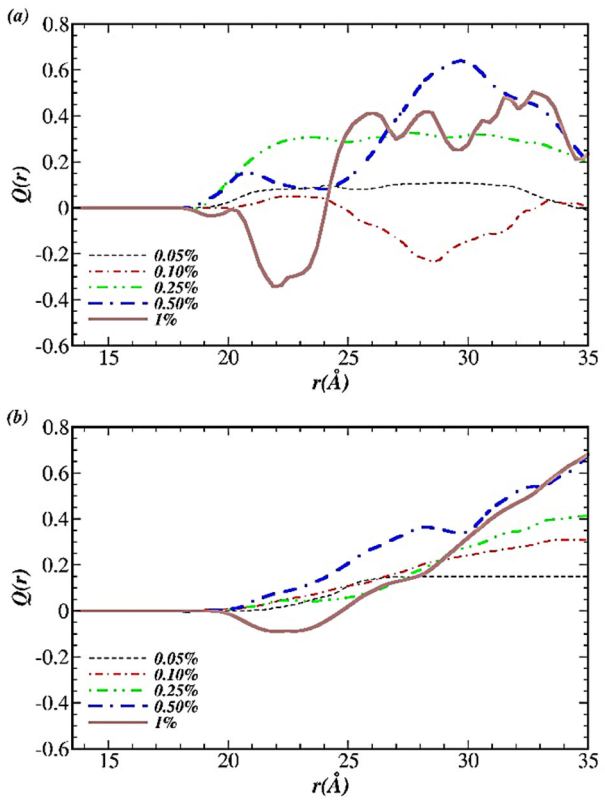

Fig. 4. Cumulative net charge for ion distribution around the NP-PEG2 in different salt (NaCl) concentrations, at (a) 300 and (b) 350 K.

for 1 wt%), but for longer r the accumulation of Na^+ ions take place. These results indicate a charge inversion at the first ion layer between 0.10 and 0.25 wt% of NaCl. At 350 K (Fig. 3b) the net charge accumulated around the NP-EG, changes significantly. Compared to 300, at 350 K the $Q(r)$ presents broad peaks and deeps, as seen in the deep at 20 Å for 0.50%, which can be interpreted as a widening of the EDL formed around the NP-EG, which can be due to the increasing in diffusivity with increasing temperature.

The $Q(r)$ results for the NP-PEG2 system at 300 and 350 K are presented in Figures 4a and 4b, respectively. As obtained for NP-EG, this temperature increase also provides an attenuation of $Q(r)$. This can be exemplified by the $Q(r)$ for all NaCl concentrations at both temperatures. The temperature increase also reduces the number and intensity of the EDLs in NP-PEG2. For example, the $Q(r)$ at 350 K (Fig. 4b) only presents an EDL for 1 wt%. On the other hand, for 300 K (Fig. 4a), the EDL is formed for salt concentrations of 0.10 and 1 wt%. However, these EDLs show inverted signals, i.e. for 0.10 wt% the layer between 20 and 25 Å presents a positive net charge (Na^+ excess), and a net negative charge (Cl^- excess) between 25 and 35 Å. A comparison of results for NP-EG and NP-PEG2 shows that the chain elongation of PEG2 provides the increase in the number of EDLs, compared to EG. This effect emerges from the Coulombic interaction between the ions with the NP core surface and the PEG functionals in the NP shell region. The silanol sites on the NP surface and the head of the PEG groups have hydrophilic character with slightly negative charge. While, the spacers (the CH_2 groups along the PEG chain) has hydrophobic character and positively charged. This configuration implies that for longer PEG chain length, the amount of charged layers will increase, as it can be seen here comparing the case with one (EG) and two (PEG2) ethylene glycol units. The data also indicate that the temperature increase reduces the number of $Q(r)$ oscillations and charge inversions at first ion layer.

3.2 Functionalized nanoparticles in brine – divalent salt ($CaCl_2$)

The effects of divalent salt in an aqueous electrolyte solution are studied in an aqueous solution with $CaCl_2$. Figures 5a and 5b present the net charge distribution as a function of the distance from the NP center of mass for 300 and 350 K, respectively. In Figure 5a, the Stern region shows substantial accumulation of positive charges (cations) for 1 wt%. This accumulation is greater than that for NP-SA at 1 wt% NaCl (Fig. 2a). This result can be explained in terms of the Coulombic interaction due to the cations. Although, Ca^{2+} and Na^+ has similar ionic radii [48], the charges differ by a factor of two. The lower

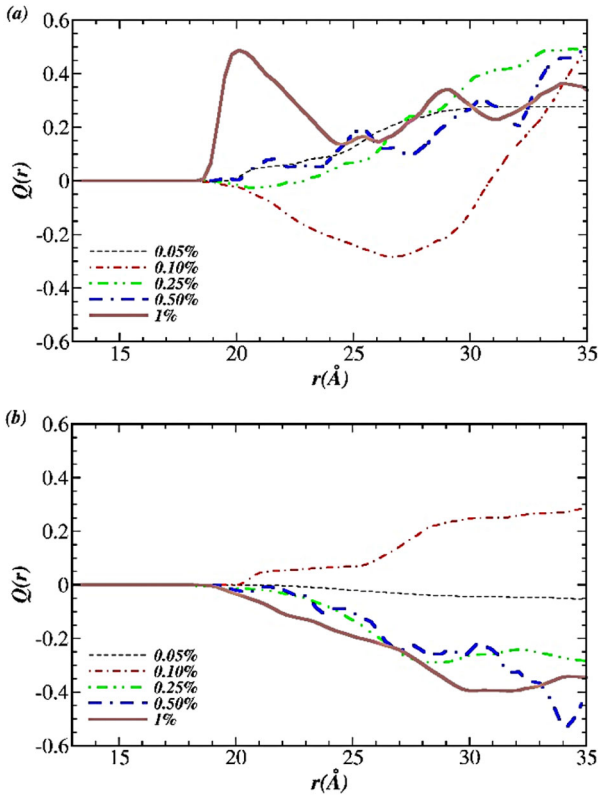

Fig. 5. The cumulative net ion charge ($Q(r)$) at (a) 300 and (b) 350 K, respectively, for an NP-SA in brine ($CaCl_2$ solutions).

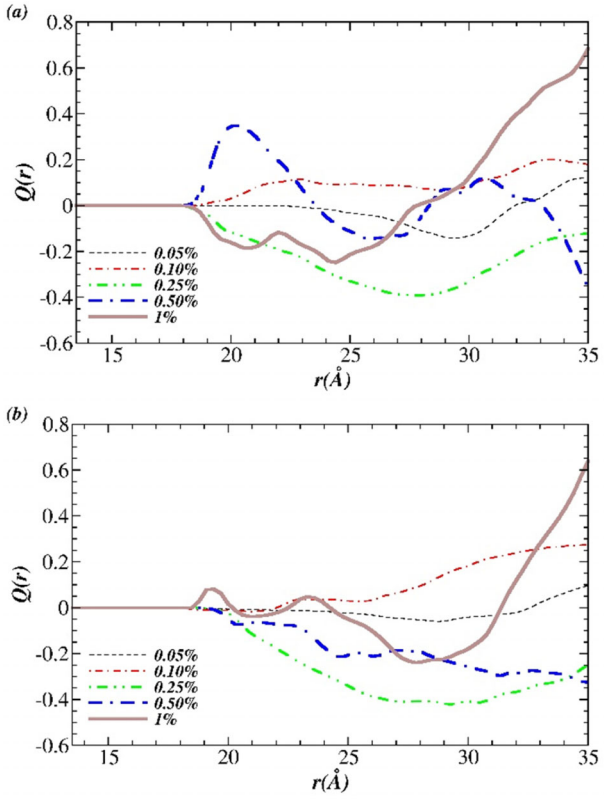

Fig. 6. The cumulative net ion charge ($Q(r)$) at (a) 300 and (b) 350 K, respectively, for an NP-EG in brine ($CaCl_2$ solutions).

charge of Na^+ ions result in a greater attenuation of the accumulation of these ions on NP surface, compared to the $CaCl_2$ solutions. As result, divalent cations such as Ca display a greater absorption effect on the NP surface than the monovalent one, as discussed in reference [13]. For $CaCl_2$ the temperature increase attenuates the $Q(r)$ intensity, as it does with the results obtained for NaCl.

The signal inversion for $CaCl_2$ is more pronounced, occurring at lower concentrations than for monovalent salts. Based on the net $Q(r)$ results, two signal inversions of the effective charge at the first ion layer are identified: one between 0.05 and 0.10 wt%, and another between 0.25 and 0.50 wt%. For a temperature of 350 K (Fig. 5b), the accumulation of cations in the Stern region is already observed at a concentration of 0.10 wt%. For concentrations of 0.05, 0.25, 0.50, and 1 wt%, the accumulation of negative charges occurs over a large extension (between 20–30 Å), defining a charge inversion between salt concentrations of 0.10 and 0.25 wt%.

The $Q(r)$ diagrams for 300 K (Fig. 5a) also provide information concerning the formation of EDLs, which occur in greater number than for monovalent salts. For example, EDLs for 0.10 and 0.25 wt% are obtained for 300 K. For divalent salts, the observed increasing in the number of EDLs occur due the compaction of the electric layers. This implies in an increase of the Coulomb interaction for this case compared with the monovalent salts. A similar effect was also observed for the hydroxilated nanoparticles [25]. The EDL for 0.10 wt% is better defined and clearly shows the prevalence of anions up to 27 Å, with a total screening at 31 Å. The presence of oscillations in the curves for 0.50 and 1 wt% also indicates the formation of unscreened charge layers around the NP. The temperature increase favors ion diffusion, and charged layers do not occur at 350 K (Fig. 5b).

The $Q(r)$ results for NP-EG at 300 and 350 K (Figs. 6a and 6b) present narrow peaks compared with NP-EG in the NaCl solution at the same temperatures (Figs. 3a and 3b). This indicates that the EDLs for divalent salts are more compact than for monovalent salts. The EDL narrowing can cause a reduction in the stability of the NP suspension, reducing the electrostatic repulsion of the system [18–20,25]. The formation of charged layers is observed at 0.05, 0.50, 1 wt% and 300 K (Fig. 6a), whereas at 350 K charged layers can be observed at 1 wt% (Fig. 6b). Compared to NaCl, the number of inversions of the effective charge at the first ion layer for $CaCl_2$ also increases. One charge inversion occurs between the concentrations of 0.10 and 0.25 wt% for NP-EG (Fig. 6a), and 0.50 and 1 wt% for NP-PEG2 (Fig. 7a) at 300 K. At 350 K, these inversions also occur for both NPs (Figs. 6b and 7b).

The spatial distance between charged layers is also reduced for NP-PEG2 in the $CaCl_2$ solution (Figs. 7a and 7b for 300 K and 350 K, respectively), compared to NaCl

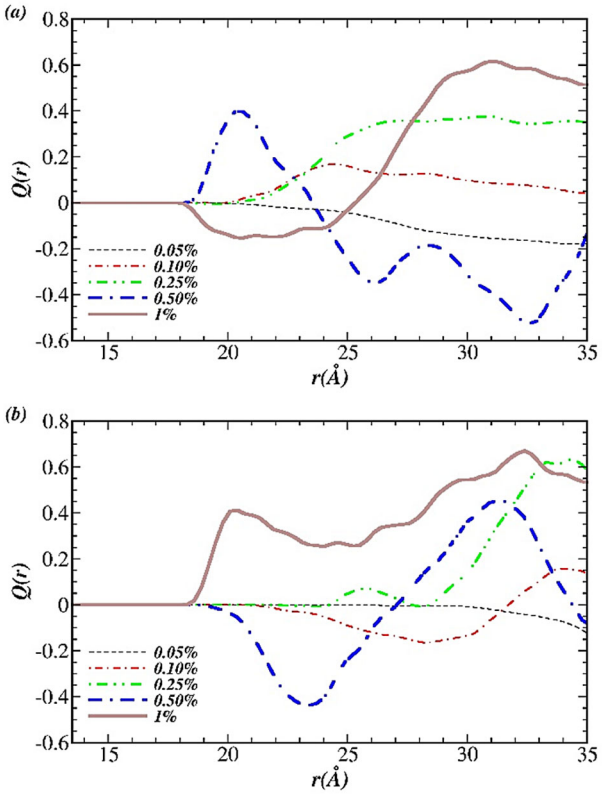

Fig. 7. The cumulative net ion charge ($Q(r)$) at (a) 300 and (b) 350 K, respectively, for an NP-PEG2 in brine ($CaCl_2$ solutions).

(Figs. 4a and 4b, for 300 and 350 K, respectively). Considering the NP-SA, NP-EG and NP-PEG2 in $CaCl_2$ solutions, some similarities between NP-SA and NP-PEG2 charge accumulation curves occur at 300 and 350 K. This happens primarily because the water solubility of both molecules (EG and PEG2) decreases with the increase of the polymer molecular weight. As a result, an initially hydrophilic EG molecule becomes hydrophobic due to the oxygen atoms along the ethylene group chain.

The formation of EDL and its narrowing provides information on the aggregation of nanoparticles. According to the DLVO (Derjaguin, Landdau, Verwey and Overbeek) theory [18–20], an electrostatic repulsion force from formed EDL stabilizes the charged particles. The results for 300 K and both salts indicate a reduction in the number of EDLs and it narrowing from NP-EG, to NP-PEG2, to NP-SA in the overall neutral NPs. The divalent salt ($CaCl_2$) increase the number of formed EDLs and reduces their thickness, compared to monovalent one (NaCl). Table 2 shows the lower salt concentration at which EDL is observed in the Stern region for different NPs. Experimentally, the maximum concentration before precipitation for NP-SA in the NaCl electrolyte solutions is 0.50 wt% at 343 K [49], while the maximum concentration for NP-SA in the $CaCl_2$ solution is 0.10 wt% at the same temperature [49]. For a PEGglyated NP the maximum concentration is 1.50 wt% of NaCl and 0.30 wt% for

Table 2. EDL formation for different functionalized nanoparticles in brine (NaCl and $CaCl_2$).

NP-SA At 300 (350) K	NP-EG At 300 (350) K	NP-PEG2 At 300 (350) K
	(wt%) NaCl	
0.25 (1.00)	0.25 (0.50)	1.00 (1.00)
	(wt%) $CaCl_2$	
0.10 (n/o)*	0.50 (1.00)	0.50 (n/o)

* n/o – not observed.

$CaCl_2$ electrolyte solutions, at 343 K [49]. The results of Table 2 are in line with the experimental ones, indicating a reciprocity between the EDL formation for charged and overall neutral NPs.

3.3 Transport properties

The transport properties for different salts were obtained for the NP-SA, NP-EG, and NP-PEG2 systems. Figure 8 shows the diffusion coefficients for the NP-SA system and different NaCl salt concentrations at 300 and 350 K. The variations in mobility depend on the temperature and the chemical species under consideration. As a general trend, the cations undergo a visibly sizeable increase in their mobility in the range of concentrations between 0 and 0.50 wt%. The mobility of Cl^- ions follows an inverse trend as function of the salt concentration and temperature, compared to Na^+ ones (especially for 350 K). This effect can be understood in terms of the Coulombic interaction of the ions with the NP-SA surface sites. At small salt concentration, the Na^+ ions can be located closer to the NP-SA surface, due to slight negative surface charge of groups and silanol sites (Fig. 1c), which implies in low mobility of the cations. The increasing salt concentration promotes an increase in the Cl^- ions concentration in the region near the NP-SA surface, reducing the anion diffusion. For salt concentrations larger than 0.50 wt%, the diffusion coefficient values appear to remain quite constant. The NPs diffusion coefficient tends to not change significantly, as it is shown in Figure 8. However, closer inspection of the diffusion coefficient shows that the NP's mobility undergoes a considerable increase, almost doubling in the salt range concentration being studied.

Figure 9 presents an enlarged view of the diffusion coefficient, where only the diffusion coefficient of the NPs is considered. For comparison, the data for the hydroxilated nanoparticle (NP-H) are also presented. All the aqueous solutions feature a steep increase in mobility for concentrations smaller than 0.2 wt%, with a decrease of the slope for the curve after this value. Similar behavior for the diffusion coefficient was found in a study performed for an NP-H as a function of the salt concentration [25]. However, in the NaCl solution, the diffusion coefficient of the NP-H is half that of the NP-SA. For divalent salt, the NP-H had similar diffusion coefficients values, as compared to those for the NP-SA. The transport properties of the NP-EG or

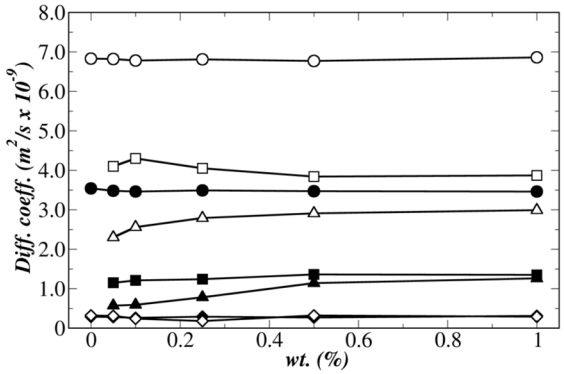

Fig. 8. Diffusion coefficients for the functionalized NP-SA and different aqueous solutions (ions and aqueous media), at 300 (solid symbol) and 350 K (clear symbol), as a function of the NaCl concentration in the solution. Symbols: circle, square, triangle, and diamond correspond to molecules, ions and NP: H_2O, Cl, Na and NP-SA, respectively.

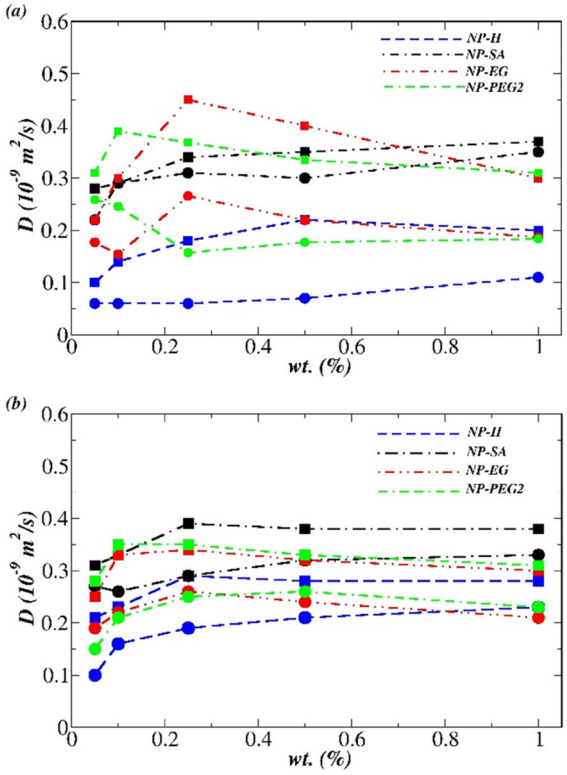

Fig. 9. Diffusion coefficient for all NPs for different concentrations and temperatures: (a) NaCl and (b) $CaCl_2$. Circles and squares correspond to 300 and 350 K, respectively.

NP-PEG2 are greater than those obtained with the NP-H in every salt concentration.

3.4 Interfacial tension

Equation (4) provides the interfacial tension values of the functionalized NPs from the three groups considered in the current study. Figures 10a and 10b show the interfacial tension data for the evaluated NPs in NaCl and $CaCl_2$ electrolyte solutions, respectively. Considering NaCl concentrations from 0 to 1 wt%, the surface tension for NP-SA varies from 1.032 N/m to 1.020 N/m at 300 K and from 1.025 N/m to 1.020 N/m at 350 K. The highest interfacial tension occurs for the NP-SA system, while the lowest value occurs with the NP-H system. For most of the electrolyte solutions and functional groups shown there is an increase in interfacial tension, with a maximum occurring at 0.10 wt%, followed by a decrease.

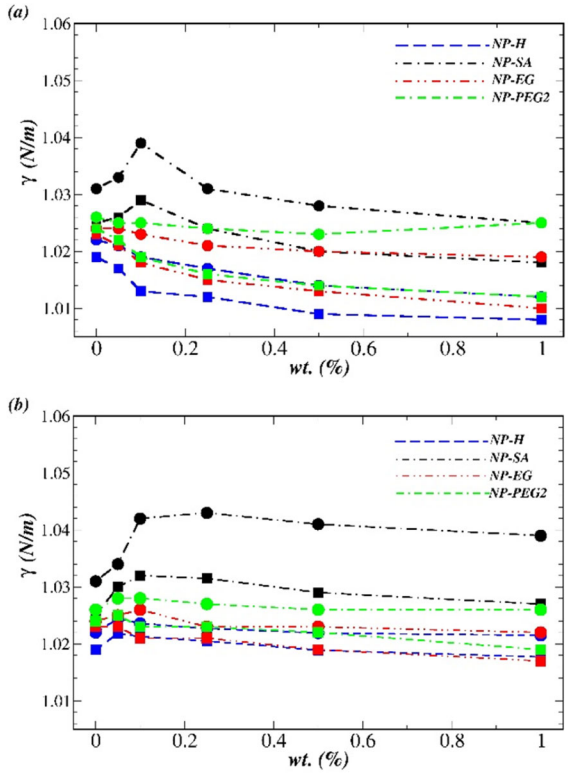

Fig. 10. Interfacial surface tension for the NPs in the (a) NaCl, and (b) $CaCl_2$ aqueous electrolyte solutions, as a function of the salt concentration and temperatures. Circles and squares correspond to temperatures of 300 and 350 K, respectively.

Considering the interfacial tension values for NP-EG and NP-PEG2 at 300 and 350 K, the surface tension increases with increasing PEG functional chains. This can be explained in terms of the hydrophobicity/hydrophilicity of groups, similarly as the effect observed on the charge distribution. Although the head of PEG groups are hydrophilic, the spacers (CH_2 groups) are hydrophobic. For longer chains, it is expected that hydrophobic characteristic prevails, changing the ions present on nanoparticles. As result, longer PEG groups attract a large number of Cl^- ions to NP surface, as shown in Figures 3 and 4. Particularly, the large amount of Cl^- ions on NP-PEG2 (Fig. 4a) result in an increase of surface tension for 1 wt% (Fig. 10a), compared to the one at 0.5 wt%. The same trend explains the large interfacial tension for NP-SA systems, in agreement with reference [50].

A large variation of interfacial tension is observed at concentrations below 0.25 wt%, while the interfacial

tension tends to be constant at concentrations greater than 0.25 wt%. The functionalization of the NP-H by EG groups gives an interfacial tension nanoparticle/brine increase of 8 mN/m for NaCl at 1 wt% and 300 K. The functionalization by PEG2 groups provides an increase of 14 mN/m under the same condition. The interfacial tension for nanoparticles in the $CaCl_2$ brine (Fig. 10b) is less than for the NaCl solution (Fig. 10a). Compared to NP-H, the NP-EG and NP-PEG2 within $CaCl_2$ 1 wt% solution at 300 K, the interfacial tension changes by 1 mN/m and 6 mN/m, respectively.

An important issue is the relationship between the interfacial tension, inversion of charge accumulation, EDL formation, and precipitation phenomena. According with experimental results for charged NPs [49], the maximum salt concentration before precipitation for NP-SA in solution with NaCl is 0.50 and 0.10 wt% for $CaCl_2$ at 343 K. The interfacial tension values for NP-SA within NaCl solution vary considerably below 0.50 wt% at 350 K (Fig. 10a). For overall neutral NP-SA in the $CaCl_2$ solution at 350 K (Fig. 10b), the interfacial tension also varies below the experimental critical salt concentration (CSC) of 0.10 wt%. Similar results are observed for the other NPs.

4 Conclusion

This study conducted molecular dynamics calculations of overall neutral silica nanoparticles (NPs) functionalized by sulphonic (SA), ethylene (EG), and polyethylene-glycol (PEG2) groups. These NPs were studied while in NaCl and $CaCl_2$ aqueous solutions, under different temperature and salt concentration conditions at constant pressure (1 atm). The net charge accumulation around the NPs was investigated for all systems, revealing some overall trends. The formation of electric double layered (EDL) systems as a function of the distance from the neutral NP, were identified in many cases. In particular, the temperature increases attenuated the EDL formation. The insertion of the functional groups (SA, EG, or PEG2) in the NP surface changes the behavior of ion absorption on the surface. The functional groups provide the increase in the number of EDLs and it narrowing from NP-EG, to NP-PEG2, to NP-AS. Compared to experimental results considering charged NPs, the EDL formation and it narrowing can indicate a similar tendency of the critical salt concentration (CSC) before the precipitation of overall neutral nanoparticles. The interfacial tension values in NaCl solutions have a high variation below the experimental CSC, at close temperatures. A similar behavior occurs for $CaCl_2$ solutions. These results show that the effects of the EDL formation and interfacial tension variation in overall neutral NP solutions are in line with that for highly charged NPs.

This work was supported by the Advanced Energy Consortium: http://www.beg.utexas.edu/aec/. Member companies include BP America Inc., BG Group, Petrobras, Repsol, Schlumberger, Statoil, Shell, and Total. The authors also acknowledge the financial support provided by the Brazilian agencies CAPES, CNPq, and Fapesp and the computational support from CENAPAD/SP, UTFPR, campus Cornélio Procópio and UFABC.

References

1. Y.-S. Lin, K.R. Hurley, C.L. Haynes, J. Phys. Chem. Lett. **3**, 364 (2012)
2. M. Xie, H. Shi, K. Ma, H. Shen, B. Li, S. Shen, X. Wang, Y. Jin, J. Colloid Interface Sci. **395**, 306 (2013)
3. J.E. Lee, N. Lee, T. Kim, J. Kim, T. Hyeon, Acc. Chem. Res. **44**, 893 (2011)
4. H. Ogihara, J. Okagaki, T. Saji, Langmuir **27**, 9069 (2012)
5. H. Ogihara, J. Xie, J. Okagaki, T. Saji, Langmuir **28**, 4605 (2012)
6. H. Ogihara, J. Xie, T. Saji, J. Colloid Interface Sci. **437**, 24 (2015)
7. G.Y. Bae, B.G. Min, Y.G. Jeong, S.C. Lee, J.H. Jang, G.H. Koo, J. Colloid Interface Sci. **337**, 170 (2009)
8. Y. Zhao, Y. Tang, X. Wang, T. Lin, Appl. Sur. Sci. **256**, 6736 (2010)
9. L. Gao, J. He, J. Colloid Interface Sci. **396**, 152 (2013)
10. Z. Guo, W. Liu, B.-L. Su, J. Colloid Interface Sci. **353**, 335 (2011)
11. X. Zhang, Y. Guo, Z. Zhang, P. Zhang, Appl. Sur. Sci. **258**, 7907 (2012)
12. D. Jiao, S. Zheng, Y. Wang, R. Guan, B. Cao, Appl. Sur. Sci. **257**, 5720 (2011)
13. C.O. Metin, L.W. Lake, C.R. Miranda, Q.P. Nguyen, J. Nanopart. Res. **13**, 839 (2011)
14. H.-Q. Sun, L. Zhang, Z.-Q. Li, L. Zhang, L. Lou, S. Zhao, Soft Matter **7**, 7601 (2011)
15. C.O. Metin, J.R. Baran Jr, Q.P. Nguyen, J. Nanopart. Res. **14**, 1246 (2012)
16. L.S. Lara, M.F. Michelon, C.O. Metin, Q.P. Nguyen, C.R. Miranda, J. Chem. Phys. **136**, 164702 (2012)
17. P. McElfresh, M. Wood, D. Ector, in *2012 SPE International Oilfield Nanotechnology Conference and Exhibition, Noordwijk, The Netherlands, 12–14 June, 2012*
18. G. Cao, in *Nanostructures and Nanomaterials*, 1st edn. (Imperial College Press, London, 2004)
19. J.M. Pettibone, D.M. Cwiertny, M. Scherer, V.H. Grassian, Langmuir **24**, 6659 (2008)
20. I.A. Mudunkotuwa, V.H. Grassian, J. Am. Chem. Soc. **132**, 14986 (2010)
21. S. Jenkins, S.R. Kirk, M. Persson, J. Carlen, Z. Abbas, J. Colloid Interface Sci. **339**, 351 (2009)
22. S. Jenkins, S.R. Kirk, M. Persson, J. Carlen, Z. Abbas, J. Chem. Phys. **128**, 164711 (2008)
23. S. Jenkins, S.R. Kirk, M. Persson, J. Carlen, Z. Abbas, J. Chem. Phys. **127**, 224711 (2007)
24. A. Dukhin, S. Dukhin, P. Goetz, Langmuir **21**, 9990 (2005)
25. L.S. de Lara, V.A. Rigo, M.F. Michelon, C.O. Metin, Q.P. Nguyen, C.R. Miranda, J. Phys.: Condens. Matter **27**, 325101 (2015)
26. J. Lyklema, Adv. Colloid Interface Sci. **147-148**, 205 (2009)
27. M. Mancui, E. Ruckenstein, Adv. Colloid Interface Sci. **105**, 63 (2003)
28. M. Mancui, E. Ruckenstein, Adv. Colloid Interface Sci. **112**, 109 (2004)

29. J.M.D. Lane, A.E. Ismail, M. Chandross, C.D. Lorenz, G.S. Grest, Phys. Rev. E **79**, 050501(R) (2009)
30. V.A. Rigo, L.S. de Lara, C.R. Miranda, Appl. Sur. Sci. **292**, 742 (2014)
31. H.R. Sondjaja, T.A. Hatton, K.C. Tam, Langmuir **24**, 8501 (2008)
32. S. Plimpton, J. Comput. Phys. **117**, 1 (1995)
33. E.R. Cruz-Chu, A. Aksimentiev, K. Schulten, J. Phys. Chem. **110**, 21497 (2006)
34. H.A. Lorentz, Ann. Phys. **248**, 127 (1881)
35. D. Berthelot, C.R. Acad. Sci. **126**, 1703 (1898)
36. J. Alejandre, G.A. Chapela, F. Bresme, J.-P. Hansen, J. Chem. Phys. **130**, 174505 (2009)
37. S. Gavryushov, J. Phys. Chem. B **111**, 5264 (2007)
38. D. Makimura, C. Metin, T. Kabashima, T. Matsuoka, Q.P. Nguyen, C.R. Miranda, J. Mater. Sci. **45**, 5084 (2010)
39. A.P. Thompson, S.J. Plimpton, W. Mattson, J. Chem. Phys. **131**, 154107 (2009)
40. R.W. Hockney, J.W Eastwood, *Computer Simulations Using Particles* (Adam Hilger, Bristol, New York, 1989)
41. S. Nosé, J. Chem. Phys. **81**, 511 (1984)
42. W.G. Hoover, Phys. Rev. A **31**, 1695 (1985)
43. H.C. Andersen, J. Chem. Phys. **72**, 2384 (1980)
44. R. Qiao, N.R. Aluru, Phys. Rev. Lett. **92**, 198301 (2004)
45. I.V. Schweigert, K.E.J. Lehtinen, M.J. Carrier, M.R. Zachariah, Phys. Rev. B **65**, 235410 (2002)
46. T. Hawa, M.R. Zachariah, J. Chem. Phys. **121**, 9043 (2004)
47. S.M. Thompson, K.E. Gubbins, J.P.R.B. Walton, R.A.R. Chantry, J.S. Rawlinson, J. Chem. Phys. **81**, 530 (1984)
48. C.D. Lorenz, A. Travesset, Phys. Rev. E **75**, 061202 (2007)
49. C.O. Metin, Ph.D. thesis, University of Texas, Austin, 2012
50. C.R. Miranda, L.S. de Lara, B.C. Tonetto, in *Proceedings of the SPE International Oilfield Nanotechnology Conference, Noordwijk, Netherlands, June 12–14, 2012*